

X-ray Spectral Variability and Rapid Variability of the Soft X-ray Spectrum Seyfert 1 Galaxies Akn 564 and Ton S180

Rick Edelson^{1,2}, T. J. Turner^{3,4}, Ken Pounds², Simon Vaughan^{2,5}, Alex Markowitz¹, Herman Marshall⁶, Paul Dobbie², Robert Warwick²

rae@astro.ucla.edu

ABSTRACT

The bright, soft X-ray spectrum Seyfert 1 galaxies Akn 564 and Ton S180 were monitored for 35 days and 12 days respectively with *ASCA* and *RXTE* (and *EUVE* for Ton S180). These represent the most intensive X-ray monitoring of any such soft spectrum Seyfert 1 to date. Light curves were constructed for Ton S180 in six bands spanning 0.1–10 keV and for Akn 564 in five bands spanning 0.7–10 keV. The short time scale (hours–days) variability patterns were very similar across energy bands, with no evidence of lags between any of the energy bands studied. The fractional variability amplitude was almost independent of energy band, unlike hard spectrum Seyfert 1s, which show stronger variations in the softer bands. It is difficult to simultaneously explain soft Seyferts stronger variability, softer spectra, and weaker energy-dependence of the variability relative to hard Seyferts.

There was a trend for soft and hard band light curves of both objects to diverge on the longest time scales probed (\sim weeks), with the hardness ratio showing a secular change throughout the observations. This is consistent with the fluctuation power density spectra that showed relatively greater power on long time scales in the softest bands. The simplest explanation of all of these is that two continuum emission components are visible in the X-rays: a relatively hard, rapidly-variable component that dominates the total spectrum and a slowly-variable soft excess that only shows up in the lowest energy channels of *ASCA*. Although it would be natural to identify the latter component with an accretion disk and the former with a corona surrounding it, a standard thin disk

¹Astronomy Department; University of California; Los Angeles, CA 90095-1562; USA

²X-ray Astronomy Group; Leicester University; Leicester LE1 7RH; United Kingdom

³Laboratory for High Energy Astrophysics; Code 660; NASA/Goddard Space Flight Center; Greenbelt, MD 20771; USA

⁴Joint Center for Astrophysics; Physics Department; University of Maryland Baltimore County; 1000 Hilltop Circle; Baltimore, MD 21250; USA

⁵Institute of Astronomy; Madingley Road; Cambridge CB3 0HA; United Kingdom

⁶Center for Space Research; Massachusetts Institute of Technology; 77 Massachusetts Ave.; NE80; Cambridge, MA 02139; USA

could not get hot enough to radiate significantly in the *ASCA* band, and the observed variability time scales are much too short. It also appears that the hard component may have a more complex shape than a pure power-law.

The most rapid factor of 2 flares and dips occurred within ~ 1000 sec, in Akn 564 and a bit more slowly in Ton S180. The speed of the luminosity changes rules out viscous or thermal processes and limits the size of the individual emission regions to $\lesssim 15$ Schwarzschild radii (and probably much less), that is, to either the inner disk or small regions in a corona.

Subject headings: galaxies: active — galaxies: individual (Akn 564) — galaxies: individual (Ton S180) — galaxies: Seyfert — X-rays: galaxies

1. Introduction

Seyfert 1 galaxies and quasars are the most powerful sustained, coherent, quasi-isotropic luminosity sources known, but their distances are so large that the “central engines” in which the luminosity is actually generated are thought to be orders of magnitude too small to image from Earth. Therefore, we must rely on indirect probes such as X-ray variability to infer information about the physical conditions in Seyfert 1s. This is potentially of general interest, because the luminosity is ultimately believed to originate in the region of strong gravity ($\lesssim 3R_S$) around a supermassive (10^6 – $10^9 M_\odot$) black hole, conditions that are unlikely to be reproduced in the laboratory in the foreseeable future.

Ultraviolet and optical emission-line variability “reverberation mapping” studies have yielded key information about the size and structure of the (much larger) broad-line regions of Seyfert 1s (see Netzer & Peterson 1997 for a review) that may allow estimation of the mass of the putative central black hole (Wandel, Peterson & Malkan 1999). Although Seyfert 1s are much more strongly variable in the X-rays, less spectacular results have been seen at those higher energies, quite possibly because the X-rays probe the smallest size/time scales which may still lie beyond the limit of current instrumentation. In recent *Advanced Satellite for Cosmology and Astronomy* (*ASCA*) and *Rossi X-ray Timing Explorer* (*RXTE*) surveys, Nandra et al. (1997), Turner et al. (1999a) and Markowitz & Edelson (2001) found evidence that variations in Seyfert 1s were the largest at softer X-ray energies. This suggests either that there are two X-ray continuum emission components, with the softer one showing stronger variability than the harder one, or that the spectrum of a single component is not constant, becoming softer as the source brightens.

Evidence for interband lags within the X-rays is less clear cut. In simultaneous *Extreme Ultraviolet Explorer* (*EUVE*), *ASCA* and *RXTE* observations of NGC 5548 and MCG-6-30-15, Chiang et al. (1999) and Reynolds (1999) respectively reported evidence that the variations in the hard X-rays consistently lagged behind those in the soft X-rays by times shorter than or of order an single spacecraft orbit. However, Edelson et al. (2000) found no such effect in intensive

RXTE monitoring of NGC 3516, and called into question the reality of lag measurements on time scales shorter than or of order the orbital time scale. If such hard interband lags are confirmed, causality arguments would require rejection of “reprocessing” models in which the soft X-rays are “secondary” emission produced by passive reradiation of “primary” hard X-ray photons.

Almost all of these studies have involved what could be called “hard X-ray spectrum Seyfert 1 galaxies” (or just “hard Seyferts”): Seyfert 1s with 2–10 keV power-law slopes in the range $\Gamma \approx 1.7 - 2.0$. These sources dominate most X-ray samples, e.g., almost all of the Piccinotti et al. (1982) Seyfert 1s are hard Seyferts. However, it is now clear that there is a significant population of Seyfert 1s with much steeper X-ray spectra ($\Gamma \approx 2.1 - 2.6$), and particularly strong (excess) emission below ~ 2 keV. Many of these “soft X-ray spectrum Seyfert 1 galaxies” (or “soft Seyferts”) are also optically classified as “narrow-line” Seyfert 1 galaxies (Osterbrock & Pogge 1985; Boller, Brandt & Fink 1996). However, it is their strongly-variable, steep soft X-ray continua that really set these objects apart; extreme examples show giant X-ray flares (as large as a factor of 100) on time scales of days (e.g., Boller et al. 1997). This rapid X-ray variability also extends to harder X-rays (Turner et al. 1999a; Leighly 1999).

The currently favored model is that soft Seyferts are powered by black holes of relatively low mass (compared to hard Seyferts of the same luminosity), accreting at a much higher rate, closer to the Eddington limit (Pounds, Done & Osborne 1995). In this model the steep X-ray spectrum is a result of enhanced emission from the putative accretion disk, and the rapid variability results from the smaller size scales associated with a lower mass black hole (Pounds et al. 2001) and perhaps also an intrinsically less stable accretion flow.

This paper reports on the most intensive X-ray monitoring of any soft Seyferts to date: a 35 day simultaneous *ASCA* and *RXTE* observation of Akn 564, and a 12 day simultaneous *ASCA*, *RXTE* and *EUVE* observation of Ton S180. This paper focuses on the X-ray spectral variability and interband lags in both objects; other results are reported elsewhere. The observations and data reduction are reported in the next section, temporal analyses are performed and discussed in § 3, the scientific implications are discussed in § 4, and a brief summary is given in § 5.

2. Observations and Data Reduction

2.1. Akn 564

Akn 564 is the brightest known soft Seyfert in the hard X-ray sky ($F_{2-10 \text{ keV}} \approx 2-5 \times 10^{-11} \text{ erg cm}^{-2} \text{ sec}^{-1}$) with a steep X-ray spectrum both above ~ 2 keV ($\Gamma \approx 2.6$) and at lower energies (Vaughan et al. 1999a; Turner, George & Netzer 1999b; Pounds et al. 2001). Unfortunately, it has rather large foreground Galactic absorption ($N_H = 6.4 \times 10^{20} \text{ cm}^{-2}$; Dickey & Lockman 1990) that prevents it from being observed with *EUVE*. In the observations reported herein, Akn 564 was observed simultaneously with *ASCA* over 2000 June 1 – July 5, with *RXTE* over 2000 June 1 –

July 1, surrounded by a total of \sim 2 yr of *RXTE* monitoring once every \sim 4.3 day. Initial results on the *RXTE* fluctuation power density spectrum (PDS) and long/short term variability have been reported in Pounds et al. (2001), and on the *ASCA* spectrum in Turner et al. (2001b), and other results will be forthcoming.

2.1.1. *ASCA* Data

ASCA has two solid-state imaging spectrometers (SISs; Burke et al. 1994) and two gas imaging spectrometers (GISs; Ohashi et al. 1996) yielding data over an effective bandpass \sim 0.7–10 keV. These data were gathered in 1CCD mode. All the data were screened according to the following criteria: the source was outside the SAA, the angular offset from the nominal pointing position was $\leq 0.01^\circ$, the RBM was ≤ 500 , the cutoff rigidity was ≤ 6 GeV/c, the source was at least 10° above the Earth’s limb (5° for the GIS) and at least 20° from the bright Earth, and the observations were made ≥ 50 s before or after passage through the terminator. These are the same methods and screening criteria used by the *Tartarus* (Turner et al. 1999a) database. This resulted in an effective exposure of 1.245 Msec in the GISs, and 1.109 Msec in the SISs. Light curves were extracted using source events within extraction cells of radii $4.8'$ and $6.6'$ for the SIS and GIS data, respectively. In order to increase the signal-to-noise ratio in the light curves, data from the SIS pair and GIS pair of detectors were (separately) combined, requiring all time bins to be at least 99% exposed. The background was subtracted from these light curves.

2.1.2. *RXTE* Data

Akn 564 was observed once every \sim 3.2 hr (= 2 orbits) during this period. The *RXTE* Proportional Counter Array (PCA) consists of five collimated Proportional Counter Units (PCUs), nominally sensitive to 2–60 keV X-rays (Jahoda et al. 1996). However, only one PCU (number 2) was in use during this campaign. The present analysis is restricted to the 2–10 keV band, where the PCA is most sensitive and the systematic errors are best understood. Data from the top (most sensitive) layer of the PCU array were extracted using the REX reduction script⁷. Poor quality data were excluded on the basis of the following acceptance criteria: the satellite has been out of the South Atlantic Anomaly (SAA) for at least 20 min; Earth elevation angle $\geq 10^\circ$; offset from optical position of Akn 564 $\leq 0.02^\circ$; and ELECTRON2 ≤ 0.1 . This last criterion removes data with high anti-coincidence rate in the propane layer of the PCA. These selection criteria typically yielded \sim 1 ksec good exposure time per orbit. The background was estimated using the “L7–240” model⁸, which is currently the best available but known to exhibit anomalies that affect AGN variability

⁷See <http://heasarc.gsfc.nasa.gov/docs/xte/recipes/rex.html>

⁸See <http://lheawww.gsfc.nasa.gov/~keith/dasmith/rossi2000/index.html>

studies (e.g., Edelson & Nandra 1999). Data were initially extracted with 16 sec time resolution.

2.2. Ton S180

The X-ray spectrum of Ton S180 is steep ($\Gamma \approx 2.4$) and, like Akn 564 shows a strong excess at lower energies (Vaughan et al. 1999; Turner et al. 2001a). Although it is not as bright as Akn 564 in the hard X-rays, it does have a much lower column ($N_H = 1.5 \times 10^{20} \text{ cm}^{-2}$; Stark et al. 1992), making possible *EUVE* observations. Ton S180 was observed simultaneously for 12 days with *EUVE*, *RXTE* and *ASCA* (as well as other telescopes) during 1999 December 3 – 15. (The *EUVE* and *RXTE* observations extended considerably beyond this period but, for consistency, this paper restricts itself to the 12 day period during which all three telescopes were operating.) Initial results on the *Chandra* spectrum have been reported in Turner et al. (2001a) and the spectral energy distributions will be forthcoming (Romano et al. 2001).

2.2.1. *ASCA* and *RXTE* Data

The *RXTE* observations of Ton S180 utilized PCUs 0 and 2. Data were extracted from these as described in § 2.1.2., the only differences being in two of the selection criteria. The TIME_SINCE_SAA criterion was extended to exclude all data taken in the 30 minutes following SAA passage. (The more conservative limit was because Ton S180 is fainter than Akn 564 and thus more susceptible to errors in background subtraction.) An ELECTRON0 ≤ 0.1 criteria was used to eliminate periods of high background.

The *ASCA* on-source exposures were 327 ksec for the SISs and 396 ksec for the GISSs. The *ASCA* data were reduced and light curves constructed using the same methods as for Ark 564, except that in this case the predominant SIS datemode was BRIGHT.

2.2.2. *EUVE* Data

A light curve was extracted from the *EUVE* deep survey (DS) data using the IRAF subpackage XRAY PROS. Source counts were summed in a circular aperture of 25 pixels in radius and the background calculated from a surrounding annulus of 30 pixels in width. In some previous analyses of *EUVE* DS light curves (e.g., Marshall et al. 1996), data with a deadtime-Primsching correction (DPC) factor > 1.25 were discarded. This correction factor accounts for the loss of events due to detector deadtime and the limited telemetry bandwidth. As the detector count rate increases, the DPC factor increases and systematic uncertainties also increase due to incomplete instrument modeling. However, during the course of reducing these data it was noted that the DS DPC factor frequently was above 1.5, significantly greater than the more typically observed values of 1.0–1.3.

This is most likely due to increased geocoronal emission possibly associated with the solar maximum and/or decreasing orbital altitude of *EUVE*. Data were therefore selected between the more liberal limits of $1.0 < DPC < 2.0$. The initial light curve was binned at 50 sec.

2.3. Long Time Scale Light Curve Construction

The observing logs are given in Table 1. Essentially identical procedures were used to construct all light curves for both objects. Data were extracted in the following subbands: 0.1–0.2 keV (for *EUVE*), 0.7–0.95 keV (for the *ASCA* SIS), 0.95–1.3 keV (for the *ASCA* SIS and GIS), 1.3–2 keV (for the *ASCA* SIS and GIS), 2–4 keV (for the *ASCA* SIS and GIS and *RXTE*) and 4–10 keV (for the *ASCA* SIS and GIS and *RXTE*). Data were then binned by the ~ 95 min orbit (or, in the case of the *RXTE* observations of Akn 564, every other orbit), and the mean and standard errors computed. This yielded light curves with 142–181 points in 12 days for Ton S180 (some were lost due to instrument problems or scheduling conflicts) and 518–520 points in 35 days for Akn 564 (231 points for *RXTE*).

Light curves taken with different instruments but in the same bands were tested for consistency. In each panel of Figure 1, the data from two different instruments were plotted in the same graph, after first dividing by the mean. As the light curves covered the same bands, they should be nearly identical, modulo the errors, sampling details, and slight mismatches in energy response. Confining the analysis first to the *ASCA* SIS and GIS data, note that the light curves show excellent agreement in both the 2–4 keV and 4–10 keV bands. (The agreement is similarly good in both sets of softer bands as well.) This gives confidence in the data and therefore the light curves were summed to produce a single *ASCA* light curve in each band where the GIS and SIS overlap, as shown in the second half of Figure 1 and in Tables 2 and 3.

Then, these summed data were compared to *RXTE* data in the same bands. Unfortunately, the *RXTE* and *ASCA* light curves do not show such good agreement. Due to its large collecting area, *RXTE* is superior to *ASCA* for monitoring the brightest 2–10 keV sources (see, e.g., Edelson et al. 2000). However, *RXTE* has a harder spectral response than *ASCA*, so the count rates are lower for soft Seyferts. Because *RXTE* is also a non-imaging instrument with a high background, the background must be modeled. As this estimated background level is larger than the mean count rate for soft Seyferts but smaller than the mean count rate for many hard Seyferts, small errors in the background model would thus cause proportionally larger problems for soft Seyferts. Indeed, Tables 2 and 3 show that the *RXTE* data for both Akn 564 and Ton S180 have both higher count rates and larger fractional errors in the 4–10 keV band than in the 2–4 keV band, which would not be expected if only Poisson statistics contributed to the errors. Because of this problem, it was decided that the *RXTE* data were not sufficiently reliable for this analysis, and they will not be scientifically analyzed in this paper. Instead, the summed *ASCA* SIS + GIS data are used, except where the paper specifically states otherwise (e.g., § 3.3.). The resulting light curves are shown in Figure 2.

2.4. Short Time Scale Light Curve Construction

These data were also used to study variations on the shortest accessible time scales: within a single *ASCA* orbit. These usually lasted 30–40 min without interruption, although a substantial minority of orbits were affected by SAA passage or minor telescope problems.

For this purpose, sets of eight 16 sec points were used to measure both the total 0.7–10 keV count rate and the 2–10 keV/0.7–1.3 keV hardness ratio. Standard methods were used to determine the mean and standard error for each quantity in each 128 sec bin. Akn 564 showed variations of a factor of 2 or larger in 16 orbits. These data are presented in Figure 3, and will be discussed in § 3.4. The largest single-orbit variations seen in Ton S180 were four orbits in which the peak-to-trough variations were 70%–85%; these will be discussed in Romano et al. (2001).

3. Temporal Analysis

In the following section the statistical properties of these light curves are examined in order to quantify any spectral variability. A complementary analysis, that of direct spectral fitting to time-resolved data, was presented in Turner et al. (2001).

3.1. Long Time Scale Fractional Variability as a Function of Energy

The fractional variability amplitude (F_{var}), a common measure of the intrinsic variability amplitude that corrects for the effects of measurement noise, is defined as

$$F_{var} = \frac{1}{\langle X \rangle} \sqrt{S^2 - \langle \sigma_{err}^2 \rangle}, \quad (1)$$

where S^2 is the total variance of the light curve, $\langle \sigma_{err}^2 \rangle$ is the mean error squared and $\langle X \rangle$ is the mean count rate (see, e.g., Edelson, Krolik & Pike 1989). The error on F_{var} is

$$\sigma_{F_{var}} = \frac{1}{2F_{var}} \sqrt{\frac{1}{N} \frac{S^2}{\langle X \rangle^2}} \quad (2)$$

as discussed in the Appendix.

Tables 2 and 3 summarize the fractional variability for each band/instrument, for Akn 564 and Ton S180, respectively. The fractional variability is also shown as a function of observing energy in Figure 4. Note that the variability amplitude is only weakly anticorrelated with energy. This is very different from the situation in more “normal” hard Seyfert 1s (see references in § 1), which tend to show stronger variability at softer X-ray energies. This will be discussed in § 4.

Again, note that the *RXTE* data show a behavior which is different than that seen in either of the *ASCA* instruments. The F_{vars} are significantly higher for the *RXTE* bands, and in fact for

Ton S180 are seen to increase with energy. This apparently spurious *RXTE* result was reported (for Akn 564) by Edelson (2000a). Based on the comparison with *ASCA*, we now believe it was almost certainly due to problems with the *RXTE* background.

The *EUVE* data on Ton S180 appear to show a downturn relative to extrapolation from the harder *ASCA* bands. However, the *EUVE* data are somewhat suspect because they are much noisier than, e.g., a factor of 4 worse than the *ASCA* data, as well as for reasons given in the next section.

3.2. Short Time Scale Fractional Variability as a Function of Energy

F_{var} measures the variability power of the total light curve. As AGN have “red” PDS (e.g., Edelson & Nandra 1999), this quantity is dominated by variations on the longest time scales probed by a given observation (e.g., Markowitz & Edelson 2001). The short time scale variability can be probed by a related parameter, called the point-to-point fractional variability (F_{pp}), defined as

$$F_{pp} = \frac{1}{\langle X \rangle} \sqrt{\frac{1}{2(N-1)} \sum_{i=1}^{N-1} (X_{i+1} - X_i)^2 - \langle \sigma_{err}^2 \rangle} \quad (3)$$

where X_i is the flux for the i th of N orbits. This measures the variations between adjacent orbits. This quantity is very similar to the “Allan Variance”⁹.

For white noise, F_{pp} and F_{var} give the same value, as we have confirmed by measuring these quantities for light curves in which the times have been randomized (to yield a white-noise PDS). However, for red noise, F_{var} will be larger than F_{pp} , as the variations will be larger on longer time scales. These quantities are tabulated in Tables 2 and 3 and shown in Figure 4.

The Ton S180 *EUVE* point is formally not defined, as the measured variability is slightly weaker than just that expected from the errors alone. This again suggests that the *EUVE* errors are not reliable and the *EUVE* F_{var} and F_{pp} values should not be taken seriously.

3.3. Similarities/Differences between Long and Short Time Scale Light Curves in Different Bands

The complex nature of the spectral variability of these objects is concisely illustrated in Figure 5. Both objects show strong orbit-to-orbit variability in the hardness ratio ($HR = F_{2-10\text{keV}}/F_{0.7-1.3\text{keV}}$). Furthermore, the hardness ratio shows a long-term secular trend for both objects. In Akn 564, it changed over 32 days from 0.527 ± 0.005 at the beginning of the monitoring to 0.604 ± 0.008 at the end, and in Ton S180, it changed over 9 days from 0.588 ± 0.007 at the beginning to 0.654 ± 0.009

⁹See <http://www.allanstime/AllanVariance/index.html>

at the end. (Mean hardness ratios and standard errors were determined by binning up hardness ratios in the first and last 3 day periods.) This is the first time such a clear difference between long and short time scale variability has been seen in different bands in a Seyfert 1 galaxy. The implications of this are discussed in § 4.

3.4. Rapid Flares and Dips

It is also interesting to examine the largest and most rapid flux and spectral flares and dips. The Akn 564 data are more well-suited for this because that source showed larger variations and the duration of the observation was almost 3 times that of Ton S180. Of the 518 useful orbits in the Akn 564 monitoring, 256 have 15 or more 128 sec bins (that is, ≥ 32 min of data). Of these 256 orbits, 15 (6%) show peak-to-trough variations of a factor of ≥ 2 (see Figure 3), and 143 (56%) show changes of $\geq 50\%$. (The fourth panel in Figure 3 has only 11 points.) That indicates that the source flux will typically change by a factor of 2 within ~ 3000 sec, and the fastest factor of 2 variations occur on very short time scales, ~ 1000 sec. In some flares (e.g., the third panel in Figure 3), the source appears to systematically harden as the flux increases and soften as the flux declines, in others (e.g., the eighth), it appears to harden as the flux decreases, and in yet others (e.g., the fifteenth), no clear trend is apparent.

3.5. Fluctuation Power Density Spectra

In order to further compare the long and short time scale variations in different energy bands, PDS were measured for each *ASCA* energy band. The *EUVE* data were not used because of the large fraction ($> 20\%$) of orbits without data. The *RXTE* data were also not used in this paper for reasons mentioned earlier. However, Pounds et al. (2001) have already used the full ~ 2 years of data on Akn 564 to determine the 2–10 keV PDS over a much broader range of time scales by the technique of Edelson & Nandra (1999).

The PDS in this paper were derived using standard methods (Oppenheim & Shafer 1975, Brillinger 1981), after first creating an evenly-sampled light curve by interpolating over the few missing points (2%–3% of the data). A Welch window was applied. The zero-power and next two (very noisy) lowest-frequency points of each PDS were ignored and the remaining points binned every factor of 1.8 (0.25 in the logarithm). The PDS covered a useable frequency range of 1.94 and 1.49 decades for Akn 564 and Ton S180 respectively. Power-law models were then measured from an unweighted, least-squares fit to the logarithmically binned data. The PDS were not corrected for noise because the variability between different orbits was much larger than the Poisson noise (as shown in the previous section). The 0.85 keV and 5 keV PDS for Akn 564 and Ton S180 are shown in Figures 6a and 6b, respectively.

For Akn 564, the PDS changes monotonically from the softest (0.85 keV) band, for which

the slope of the PDS was -1.22 ± 0.06 , and the hardest (5 keV) band, for which the slope was -0.96 ± 0.07 . Similar behavior was seen in Ton S180, which had a PDS slope of -1.61 ± 0.08 at 0.85 keV and -1.18 ± 0.09 at 5 keV. In both cases the slope differences are highly significant. The sense of the difference is that the softest bands show more power on the longest time scales probed.

3.6. Fractional Variability versus Flux Level

For Akn 564, F_{vars} were also measured for each of the 256 orbits with more than 32 min of data. These were sorted by flux levels and averaged in flux bins with 20 or more points in order to smooth out fluctuations. The result is plotted as a function of mean count rate in Figure 7. The variability amplitude is quite independent of count rate over a factor of ~ 4 in count rate, which means that the intrinsic RMS amplitude (corrected for the measurement noise) is linearly correlated with flux. The implications of this result are discussed in detail in § 4.

3.7. Linearity of the Light Curves

A search for non-linear behavior (e.g., Leighly & O’Brien 1997; Green, McHardy & Done 1999) was undertaken with the Akn 564 and Ton S180 light curves. The surrogate data method of Theiler et al. (1992) was used, in which a discriminating non-linear statistic is applied both to the real data and to simulated light curves. A significant difference between the values of the statistic as computed for the real and simulated data indicates a detection of non-linearity in the real light curve. Here, the Kolmogorov-Sminov (KS) D-statistic, which compares the distribution of data points above the mean with those below the mean (e.g., Press et al. 1992), is applied to all light curves. A larger value of the D-statistic implies stronger non-linearity.

For each of the two targets, 100 simulated light curves, each with a PDS slope corresponding to the PDS slope measured for the actual data, were randomly generated using the algorithm of Timmer & König (1995). Parent light curves had 4096 data points (much more than in the observation to reduce red-noise leak) and a time resolution corresponding to 1 *ASCA* orbit. A section of the light curve corresponding to the observation length was randomly chosen and sampled in the same fashion as the actual data. The KS D-statistic was calculated for each simulated light curve, and these values were ranked.

The KS D-statistic for the summed 0.7–10 keV Akn 564 light curve was found to be greater than 86% of the KS D-statistic values for light curves simulated with PDS slope of -1.13 . The KS D-statistic for the summed 0.7–10 keV Ton S180 light curve was found to be greater than 63% of the KS D-statistic values for light curves simulated with PDS slope of -1.52 . Neither of these are $> 1.5\sigma$ effects. Thus, this test provided no evidence for non-linear variability in either of these light curves. However, tests for non-linearity (and the related non-Gaussianity) are notoriously difficult (see Press & Rybiki 1997 for a detailed discussion) so this is perhaps not as different from previous

results as it might appear.

3.8. Interband Lags

Interband lags were searched for using the cross-correlation functions: both the discrete correlation function (Edelson & Krolik 1988) and interpolated correlation function (White & Peterson 1994). The results are shown in Figure 8, and summarized in Tables 4 and 5. They confirm that all of the Akn 564 data are highly correlated, with correlation coefficients $r = 0.85$ to 0.99 , and none of the bands appears to lead another, down to $\lesssim 1$ orbit, or $|\tau| < 1.5$ hr. (The formal errors were much smaller, but we conservatively claim no limit stronger than this; see Edelson et al. 2001 for a detailed discussion of uncertainties of interband lags and the perils of “super-resolution”.) The Ton S180 data are also highly correlated, although not nearly as well as for Akn 564. These data also show no lags down to limits of $\lesssim 1$ orbit. For CCFs that do not include the *EUVE* data, correlation coefficients are $r = 0.48$ to 0.92 . The *EUVE* data is not as well correlated; for CCFs that do include the *EUVE* data, correlation coefficients were much lower: $r = 0.32$ to 0.59 .

4. Discussion

4.1. Separating Emission Components with Spectral Variability

This monitoring of the soft Seyfert 1s Akn 564 and Ton S180 on time scales of weeks revealed a number of new and interesting results: on short time scales, the variations are similar in all bands, with no measurable interband lags down to the shortest time scales measurable and no consistent trend for the spectrum to harden or soften during flares and dips. However, especially in Akn 564, the hard and soft bands appear to diverge on longer time scales, and the soft bands had slightly larger variability amplitudes that apparently resulted from a long-term trend relative to the hard bands.

It is difficult to see how a single emission component could naturally produce spectral evolution that is so markedly different on long and short time scales. Instead, the simplest explanation is that two separate continuum emission components are visible in the X-rays: the first is a rapidly-variable hard component that dominates the emission, especially at the hardest energies, for which the shape changes only weakly, hardening slightly as the total flux changes by a factor of >2 . The second is a much more slowly-variable “soft excess” component only seen in the lowest-energy channels of *ASCA*. Because it only contributes to the softest channels, these data alone cannot determine if its shape changes with time. There appears to be no obvious temporal connection between the two components.

The spectral and variability properties of the soft component are not consistent with the simplest models of direct thermal emission from an optically thick, geometrically thin accretion

disk (e.g., Frank, King & Raine 1992). Even for the most favorable realistic parameters, the disk temperature is well below 0.1 keV, while the observed emission (from the spectral fits) extends well above 1 keV. This general problem is well known (e.g., Czerny & Elvis 1989). While gravitational focussing and Comptoniation could harden the spectrum somewhat, it is difficult to see how such a strong effect could be produced. Likewise, the relevant time scale for variations in a disk is probably the viscous time scale, which for any reasonable set of parameters is years, compared with the observed variability on time scales of $\lesssim 1$ week (see also Turner et al. 2001b).

The hard component is generally identified with emission from a patchy corona (e.g., Haardt, Maraschi & Ghisellini 1994). Because the cells are relatively small compared to the overall structure, and the process could proceed as quickly as the light-crossing time (e.g., in the case of magnetic reconnection), then the expected time scales are comfortably consistent with the observed variability time scales.

However, these results are not entirely consistent with the simple picture in which the spectrally-defined fit parameters fully describe the physically relevant emission components. Turner et al. (2001b) fitted the spectrum of Akn 564 with a power-law and (Gaussian) soft excess, and found that the soft excess component faded by a factor of 2.8 throughout the observation, while the harder power-law faded by only a factor of 1.68. This is consistent with the overall hardness ratio changes reported in § 3.3. However, this slowly-varying component would be nearly constant during a single orbit, and thus would provide a constant “contamination” at soft energies during any rapid flares/dips. This would yield a correlation between hardness and flux, in the sense that the source would get harder during a flare and softer during a dip. As discussed in § 3.4., this is not the case. This means that the straightforward spectral fits do not tell the full story, and that most likely the rapidly variable component contains not only the hard component (described as a power-law) but also some of the soft excess as well. That is, the hard component appears to be intrinsically more complex than the pure power-law description used in spectral fitting routines.

4.2. Implications of Rapid Variability

Akn 564 shows factor of 2 flares and dips on time scales as short as 1000 sec. For its redshift of $z = 0.0247$ (Huchra, Vogeley & Geller 1999), this corresponds to a change in the 0.7–10 keV luminosity $\Delta L/\Delta t \approx 10^{41}$ erg/s². Under the assumptions of isotropic emission, the Eddington limit implies $M_{BH} \geq 8 \times 10^5 L_{44} M_\odot$, where L_{44} is the *bolometric* luminosity in units of 10^{44} erg sec⁻¹ (e.g., Peterson 1997). If we assume that Akn 564’s 0.6–10 keV luminosity is 10% of bolometric, then $L_{44} \approx 8$ and $M_{BH} \geq 6 \times 10^6 M_\odot$. We note that all of these assumptions mean that the limit is probably good to no better than an order of magnitude. Even so, for a black hole mass above this limit, both the radial drift/viscous and thermal processes, operating at distances of $\sim 10R_S$, give time scales that are much too long (hours to years; see Frank et al. 1992) to be compatible with the observed time scale of ~ 1000 sec. Thus, such processes cannot be responsible for the observed X-ray emission.

The light crossing time scale yields an approximate upper limit (to within the order of magnitude uncertainties discussed above) on the size of the emitting region of $R \lesssim 15R_S$ for $M_{BH} \geq 6 \times 10^6 M_\odot$ and $T = 1000$ sec. For other processes (governed, e.g., by the orbital or dynamical time scales), the upper limit on the size of the emitting region must be significantly smaller. This indicates that the bulk of the X-ray emission in Akn 564 must either be produced in the inner accretion disk or else isolated clumps that are smaller than or of order a few tens of Schwarzschild radii.

4.3. Statistical Properties of the X-ray Variability

Decomposition of the X-ray emission into two components with very different spectral shapes and variability time scales would also significantly affect the interpretation of the PDS. Recent intensive and long-term monitoring of Seyfert 1s have begun to yield evidence that the power-law PDS measured at short time scales (e.g., Lawrence & Papadakis 1993) show a turnover at longer time scales (Edelson & Nandra 2000, Pounds et al. 2001, Uttley, McHardy & Papadakis 2001). However, the shape of this turnover is unclear, and it is consistent with a variety of shapes (Uttley et al. 2001). The PDS of Galactic X-ray binaries (XRBs), for which the shapes are much better-defined than for Seyfert 1s (due to their much shorter time scales and higher fluxes) often show a more complex structure with multiple features (Nowak 2001). These multiple features could be multiple time scales, indicating that the PDS cannot be modeled by single variability component. The spectral evidence presented in this study suggests that the same situation may be the case with Seyfert 1s.

The fact that F_{var} is independent of flux level demonstrates that the light curve is non-stationarity but in a relatively “well-behaved” and repeatable fashion. This result confirms and expands upon the finding of Uttley & McHardy (2001) that found a similar independence of F_{var} from flux for three other Seyfert 1s, although those were measured with only two independent flux points. These results are consistent with no zero-point offset, indicating that source does not have a large, constant flux component. More importantly, the independence of F_{var} from flux level shows yet another remarkable parallel between Seyfert 1s and XRBs, suggesting a relationship exists between these putative accreting black hole sources independent of the mass of the central object, even though they differ by a factor of $\gtrsim 10^6$ in luminosity and black hole mass.

Finally, it is interesting that neither of these two objects show strong non-linear variability, at least using the method of Theiler et al. (1992). Although this may not be the ideal method to use, visual examination of the light curves also suggest that the variations are not wildly non-linear, as the dips are about as strong as the flares (on a logarithmic plot).

4.4. Soft and Hard Spectrum Seyfert 1 Galaxies

With the study of these two soft Seyferts, it is now becoming feasible to systematically explore the differences between the variability in soft and hard Seyferts. It is already well known that soft Seyferts tend to have narrower optical permitted emission lines (Boller et al. 1996) and that they show much stronger X-ray variability than hard Seyferts at a similar luminosity (Leighly 1999; Turner et al. 1999a). This may be more pronounced on short time scales: Pounds et al. (2000) finds that the PDS of Akn 564 is unusually flat, meaning that there is more variability power on short time scales relative to long time scales than in hard Seyferts.

This is the first study to quantify the rapid variations in individual sources: significant variations are almost always seen within a single orbit (<40 min on source), and in the best studied case, Akn 564 showed factor of two variations in $\sim 6\%$ of all well-determined orbits. This result is consistent with the idea first put forward by Pounds et al. (1995) that soft Seyferts are accreting at a much higher fraction of the Eddington rate than hard Seyferts.

A new clue that is emerging involves the spectral variability results in § 3.1.: both of these soft Seyferts show only a very weak dependence of variability amplitude on energy. Other observations of soft Seyferts appear to show the same behavior. A recent *Chandra* observation by Collinge et al. (2001) found that the soft Seyfert NGC 4051 varied in 0.5–8 keV flux by a factor of >5 in a ~ 4 ksec period while the 0.5–2 keV/2–8 keV flux ratio changed by less than 20%. Likewise, Gliozzi et al. (2001) find that the soft Seyfert PKS 0558–504 actually hardens as it gets brighter. Finally, *XMM-Newton* observations of both Ton S180 and the soft Seyfert 1H 0707–495 show strong variability with almost no energy dependence (Vaughan 2001). This is very different behavior than seen in hard Seyferts, which generally have X-ray spectra that appear to soften as they brighten (e.g., Markowitz & Edelson 2001).

It is difficult to construct unified phenomenological picture that can neatly explain all of these results. Soft Seyferts tend to have stronger soft excesses, stronger overall variability than hard Seyferts, yet hard Seyferts show much stronger energy dependence of the variations (in the sense that their spectra become softer as the flux increases). This is the opposite of what would be expected from mixing a soft (rapidly variable) and hard (less variable) component such that the former dominates in soft Seyferts and the latter in hard Seyferts. (It also contradicts the observation that the soft component appears to be the less variable one.) Likewise, if the harder component is the highly variable one, then one would expect hard Seyferts to show stronger variability than soft Seyferts. Of course, it may be that these objects are may be powered by completely different processes, and no unified scheme is applicable.

5. Summary

This paper reports the most intensive X-ray monitoring ever undertaken of any soft Seyfert galaxy. These extraordinary data sets allow a deeper and more systematic quantification of soft Seyfert variability than was previously possible. Both sources show strong variability, with Akn 564 showing repeated variations of a factor of 2 on time scales as short as ~ 1000 sec. However, these relatively well-sampled light curves do not clear evidence of non-linear behavior reported for other soft Seyferts, as the number and strength of flares and dips were comparable. The hard and soft light curves track well on short time scales, with no clear trends for the hardness ratio to change in a systematic way during a flare. On longer time scales, especially for Akn 564, the hard and soft bands diverge somewhat, yielding larger long time scale variability amplitudes in the softer bands.

The rapid variations rule out thermal and viscous processes and constrain the emission to the inner $\lesssim 15R_S$, most likely to the inner disk or small clumps in a corona. The spectral variability indicates the presence of two components, the dominant one (in the 0.6–10 keV *ASCA* band) being a hard, rapidly variable component that is naturally associated with a corona. However, the softer, more slowly variable component cannot be identified with the simplest optically thick, geometrically thin accretion disk models, as the emission is observed to extend well beyond 1 keV, and the observed variability time scales are much too short.

The variability amplitude was found to be almost independent of energy band for these objects, and there are indications that the same is true for other soft Seyferts as well. This indicates a possibly important difference with hard Seyferts, which generally show significantly softening of the spectrum as the flux increases. Other known differences between the sources is that soft Seyferts tend to be more rapidly variable and also to have narrower optical permitted lines. This is not easy to understand in terms of phenomenological models in which essentially identical hard and soft components are mixed together in different ratios to produce the two types of Seyferts, and instead appear to require a more complex explanation.

These observations show that intensive spectral variability monitoring has unique power to separate out emission components in a way that is complementary to single-epoch spectroscopy. As these objects are much too distant to image directly, spectral variability studies may prove our most effective tool for determining the processes responsible for the high X-ray luminosities of AGN. While the current *ASCA* and *RXTE* archives contain a great deal of relevant data, we expect that future progress will hinge on *XMM-Newton*. Its high throughput makes it the only instrument with sufficient sensitivity to obtain meaningful short term light curves for the most extreme and interesting soft Seyferts which tend to be almost an order of magnitude fainter than Akn 564 and Ton S180. Its broad bandpass allows it to simultaneously study spectral variations over a much larger fraction of the X-ray spectrum than was previously possible, especially at the critical soft energies (which were not probed by *ASCA* or *RXTE*). Finally, its high-Earth orbit yields uninterrupted ~ 40 hr light curves that can be used to study short time scale variability. The previous generation of low-Earth orbit telescopes produced light curves corrupted by interruptions

that made it impossible to track the development of flares. Although the ideal parameters for such observations are not yet fully determined, it is likely that more insight will be gained from a few long observations instead of many short ones (Mushotzky 2001). It is also important that future variability studies accurately define the variability properties of both soft Seyferts (especially the most extreme examples like IRAS 13224–3908, PHL 1092 and 1H 0707-495) but also of a control of group of “standard” hard Seyferts such as NGC 5548. As such long observations are unlikely to be scheduled in great numbers in this early stage of the mission (e.g., only one Seyfert 1, MCG–6-30-15, has been scheduled for more than a single orbit in the first two years of *XMM-Newton*), patience is a necessary virtue in this area of endeavor.

The authors thank the *RXTE* and *ASCA* teams for their efforts that resulted in the data needed for this research. They also thank the referee, Niel Brandt, for helping to focus the discussion on the big picture. Edelson and Markowitz were supported by NASA grants NAG 5-7317 and NAG 5-9023, and Turner was supported by NASA grant NAG 5-7385.

A. The Estimation of the Fractional Excess Variability Amplitude, F_{var} , of an AGN Light Curve

Here we present a prescription for measuring the fractional excess variability parameter F_{var} and its associated error. We also note various caveats relating to its interpretation.

A.1. Basic Equations and Derivation of F_{var}

Consider a light curve subdivided into N time bins, where each bin is further subdivided into n_i individual points (n_i can be the same or different in each bin). The mean count rate in the i th bin is:

$$X_i = \frac{1}{n_i} \sum_{j=1}^{n_i} x_{ij}, \quad (\text{A1})$$

where x_{ij} is the count rate of the j th point in the i th bin. The square of the standard error on X_i is:

$$\sigma_{err,i}^2 = \frac{1}{n_i(n_i - 1)} \sum_{j=1}^{n_i} (x_{ij} - X_i)^2. \quad (\text{A2})$$

In considering the full light curve, the unweighted mean count rate given by:

$$\langle X \rangle = \frac{1}{N} \sum_{i=1}^N X_i, \quad (\text{A3})$$

and the variance of the binned data comprising the light curve is:

$$S^2 = \frac{1}{N-1} \sum_{i=1}^N (X_i - \langle X \rangle)^2. \quad (\text{A4})$$

Both intrinsic source variability and measurement uncertainty contribute to this observed variance. Under the assumption that both components are normally distributed and combine in quadrature, the observed variance can be written as:

$$S^2 = \langle X \rangle^2 \sigma_{XS}^2 + \langle \sigma_{err}^2 \rangle \quad (\text{A5})$$

The first term on the right represents the intrinsic scatter induced by the source variability. The second term is the contribution of the measurement noise. We assume that the scatter of the data points within an individual time bin is predominantly due to the statistical uncertainty of the measurements, leading to:

$$\langle \sigma_{err}^2 \rangle = \frac{1}{N} \sum_{i=1}^N \sigma_{err,i}^2, \quad (\text{A6})$$

Rearranging equation A5 yields the standard definition for the fractional excess variance

$$\sigma_{XS}^2 = \frac{S^2 - \langle \sigma_{err}^2 \rangle}{\langle X \rangle^2}. \quad (\text{A7})$$

The fractional variability amplitude F_{var} is simply the square root of the fractional excess variance:

$$F_{var} = \sqrt{\frac{S^2 - \langle \sigma_{err}^2 \rangle}{\langle X \rangle^2}}, \quad (\text{A8})$$

as given in Equation 1 of the text.

A.2. Derivation of the Uncertainty on F_{var}

We now require a measure of the uncertainties that should be assigned to σ_{XS}^2 and F_{var} . In equation A7, assume that the dominant variance will be that associated with the quantity S^2 , and that the error term $\langle \sigma_{err}^2 \rangle$ can be neglected by comparison. The implications of this assumption are discussed at the end of this section.

This variance on S^2 can be estimated as $\frac{2}{N-1}S^4 \approx \frac{2}{N}S^4$ (e.g., Trumpler & Weaver 1962). Hence the standard deviation of σ_{XS}^2 is:

$$\sigma_{\sigma_{XS}^2} = \sqrt{\frac{2}{N} \frac{S^2}{\langle X \rangle^2}} \quad (\text{A9})$$

Setting $x = \sigma_{XS}^2$ and $y = F_{var}$ so that $y = \sqrt{x}$ yields

$$\frac{dy}{dx} = \frac{1}{2\sqrt{x}} = \frac{1}{2y} = \frac{1}{2F_{var}} \quad (\text{A10})$$

Transmitting the error through the equation by the standard formula $\sigma_y = \frac{dy}{dx}\sigma_x$ yields

$$\sigma_{F_{var}} = \frac{1}{2F_{var}}\sigma_{\sigma_{XS}^2} = \frac{1}{2F_{var}}\sqrt{\frac{1}{N} \frac{S^2}{\langle X \rangle^2}} \quad (\text{A11})$$

as in Equation 2 of the text.

In the above analysis the assumption (made in eqn. A2) that all of the variance within a time bin is due solely to measurement errors will lead to overestimation of the latter if the source exhibits rapid variability on time scales comparable to the bin size. This is a conservative approach which in many circumstances may be a better choice than relying on the errors propagated through data extraction and data fitting algorithms (which may mix systematic and statistical errors in a manner not appropriate for variability studies). The importance of such an approach can be seen in the fact that the error estimate assumed that the variance due to systematic errors was small compared to the total variance; if they are not the derivation is incorrect.

More serious, however, is the assumption that the underlying source variability is governed by processes that are stationary and governed by Gaussian statistics. As red-noise processes are “weakly non-stationary” (e.g., Press & Rybicki 1997) the above error estimate cannot account for random fluctuations in F_{var} as a function of time. A further point is that the weak non-stationarity and (in general) non-normal distribution of fluxes in red-noise light curves mean that the above prescription provides an increasingly poor estimate of the uncertainty on F_{var} as the signal-to-noise in the observed light curve increases. (This will be discussed in more detail in a future work, Vaughan et al. in prep.) A more robust approach would be to estimate the PDS, but where this is not possible F_{var} can provide a useful measure of the degree of variability in a given light curve. In practice the value of statistics such as F_{var} is as a comparative measure of the magnitude and constancy of the variability signal.

REFERENCES

- Boller, Th., Brandt, W. N., Fabian, A. & Fink, H. 1997, MNRAS, 289, 293
Brandt, W. N., Boller, Th., Fabian, A. & Ruszowski, M. 1999, ApJL, 303, L53
Brillinger, D. 1981 “Time Series: Data Analysis and Theory,” 2nd edition, (San Francisco: Holden-Day)
Burke, B., Mountain, R., Daniels, P., Dolat, V. 1994, IEEE Trans. Nuc. Sci. 41, 375
Chiang, J., Reynolds, C., Blaes, O., Nowak, M., Murray, N., Madajski, G., Marshall, H., Magdziarz, P. 1999, ApJ, 528, 292
Collinge, M. et al. 2001, ApJ, in press, astro-ph/0104125
Czerny, B. & Elvis, M. 1987, ApJ, 321, 305
Edelson, R. & Krolik, J. 1988, ApJ, 333, 646
Edelson, R. & Nandra, K. 1999, ApJ, 514, 682
Edelson, R. 2000a, New Ast Rev, 44, 423
Edelson, R. et al. 2000b, ApJ, 534, 180
Edelson, R., Griffiths, R. G., Markowitz, A., Sembay, S., Turner, M., Warwick, R. 2001, ApJ, in press, astro-ph/0102458
Fabian, A. 1979, Proc. R. Soc. London Ser. A, 336, 449
Forster, K. & Halpern, J., 1996, ApJ, 468, 565
Frank, J., King, R. A., Raine, D. J., 1992, “Accretion Power in Astrophysics,” 2nd edition (Cambridge University Press)
Gliozzi, M. et al. 2001, A&A, 365L, 128
Goodrich, R. 1989, ApJ, 342, 234
Green, A., McHardy, I. & Done, C. 1999, MNRAS 305, 309
Haardt, F., Maraschi, L. & Ghisellini, G. 1994, ApJL, 432, 95
Huchra, J., Vogeley, M. & Geller, M. 1999, ApJS, 121, 287
Jahoda, K., Swank, J., Giles, A., Stark, M., Strohmayer, T., Zhang, W., Morgan, E.H. 1996, SPIE 2808, 59
Lawrence, A. & Papadakis, I. 1993, ApJ, 414, L85
Leighly, K. & O’Brien, P. 1997, ApJ, 481, L15
Leighly, K. 1999, ApJS, 125, 317
Markowitz, A. & Edelson, R. 2001, ApJ, 547, 684
Marshall, H. et al. 1996, ApJ, 457, 169

- Mushotzky, R. 2001, in Proceedings of the JHU Workshop on Accretion Disks, ed. T. Yaqoob, in prep.
- Nandra, K., George, I., Mushotzky, R., Turner, T. J. & Yaqoob, T. 1997, ApJ, 476, 70
- Netzer, H. & Peterson, B. 1997, in Astronomical Time Series, Eds. D. Maoz, A. Sternberg & E. M. Leibowitz, (Dordrecht: Kluwer), p. 85
- Nowak, M. 2001, MNRAS, 320, 327
- Ohashi, T. et al. 1996, PASJ, 48, 157
- Oppenheim, A. & Shafer, R. 1975, “Digital Signal Processing,” (Paramus: Prentice-Hall)
- Osterbrock, D. & Pogge, R. 1985, ApJ, 297, 166
- Peterson, B. M. “An Introduction to Active Galactic Nuclei,” 1st Edition (Cambridge University Press)
- Piccinotti, G. et al. 1982, ApJ, 253, 485
- Pounds, K., Done, C. & Osborne, J. 1995, MNRAS, 277, L5
- Pounds, K., Edelson, R., Markowitz, A. & Vaughan, S. 2001, ApJ, 550, L15
- Press, W. et al. 1992, “Numerical Recipes: The Art of Scientific Computing,” 2nd Edition, (Cambridge University Press)
- Press, W. & Rybiki, G. 1997, in Astronomical Time Series, Eds. D. Maoz, A. Sternberg & E. M. Leibowitz, (Dordrecht: Kluwer), p. 61
- Reynolds, C. S. 1999, ApJ, 533, 811
- Robinson, A. 1994, ASP Conf Ser, 69, 147
- Romano, P. et al. 2001, in preparation
- Theiler, J., Eubank, S., Longtin, A., Galdrikian, B. & Farmer, J. 1992, Physica D, 58, 77
- Timmer, J. & König, M. 1995, A&A, 300, 707
- Trumpler, R. J., Weaver, H. F., 1962, “Statistical Astronomy”, New York: Dover, p190
- Turner, T. J., George, I., Nandra, K. & Turcan, D. 1999a, ApJ, 524, 667
- Turner, T. J., George, I. & Netzer, H. 1999b, ApJ, 526, 52
- Turner, T. J. et al. 2001, ApJL, in press, astro-ph/0012129
- Turner, T. J. et al. 2001b, ApJL, in press, astro-ph/0105283
- Uttley, P. & McHardy, I. 2001, MNRAS, 323, L26
- Uttley, P., McHardy, I. & Papadakis, I. 2001, MNRAS, submitted
- Vaughan, S. et al. 1999, MNRAS, 308, L34
- Vaughan, S. 2001, in Proceedings of the JHU Workshop on Accretion Disks, ed. T. Yaqoob, in prep.

- Wandel, A., Peterson, B. M. & Malkan, M. 1999, MNRAS, ApJ, 526, 579
White, R., Peterson, B. M. 1994, PASP, 106, 879

Table 1. Observing Log

Source	Instrument	Energy Range (keV)	JD Range (–2,450,000.5)	Sampling Rate (min)	Number Points
Ton S180	<i>ASCA</i> SIS	0.7 – 10	1515.55 – 1527.78	94.8	180
	<i>ASCA</i> GIS	0.95 – 10	1515.55 – 1527.78	94.8	181
	<i>EUVE</i>	0.1 – 0.2	1515.56 – 1527.79	94.1	142
	<i>RXTE</i>	2 – 10	1515.59 – 1527.72	95.8	142
Akn 564	<i>ASCA</i> SIS	0.7 – 10	1696.52 – 1731.00	94.0	518
	<i>ASCA</i> GIS	0.95 – 10	1696.52 – 1731.00	94.0	520
	<i>RXTE</i>	2 – 10	1696.63 – 1726.47	191.4	231

Table 2. Akn 564 Variability Parameters

Instrument	Energy Range (keV)	Band Center (keV)	Count Rate (c/s)	Signal to Noise	Total Variance	Fractional Variability	Point-to-Point Variability
<i>ASCA</i>	0.7 – 0.95	0.85	0.57	31.1	$34.2 \pm 1.1\%$	$34.0 \pm 1.1\%$	$14.4 \pm 0.5\%$
<i>ASCA</i>	0.95 – 1.3	1.1	1.42	43.4	$33.2 \pm 1.0\%$	$33.1 \pm 1.0\%$	$15.5 \pm 0.5\%$
<i>ASCA</i>	1.3 – 2	1.5	1.57	43.3	$33.4 \pm 1.0\%$	$33.3 \pm 1.0\%$	$15.9 \pm 0.5\%$
<i>ASCA</i>	2 – 4	2.5	0.86	33.3	$32.4 \pm 1.0\%$	$32.3 \pm 1.0\%$	$16.0 \pm 0.5\%$
<i>ASCA</i>	4 – 10	5	0.27	19.7	$30.3 \pm 0.9\%$	$29.8 \pm 1.0\%$	$16.8 \pm 0.6\%$
SIS	0.7 – 0.95	0.85	0.57	31.1	$34.2 \pm 1.1\%$	$34.0 \pm 1.1\%$	$14.4 \pm 0.5\%$
SIS	0.95 – 1.3	1.1	1.00	39.7	$33.2 \pm 1.0\%$	$33.1 \pm 1.0\%$	$15.0 \pm 0.5\%$
SIS	1.3 – 2	1.4	0.95	37.5	$33.3 \pm 1.0\%$	$33.2 \pm 1.0\%$	$15.6 \pm 0.5\%$
SIS	2 – 4	2.5	0.45	27.0	$32.6 \pm 1.0\%$	$32.4 \pm 1.0\%$	$15.8 \pm 0.5\%$
SIS	4 – 10	5	0.13	14.8	$31.2 \pm 1.0\%$	$30.4 \pm 1.0\%$	$16.4 \pm 0.6\%$
GIS	0.95 – 1.3	1.1	0.42	28.6	$33.0 \pm 1.0\%$	$32.8 \pm 1.0\%$	$15.1 \pm 0.5\%$
GIS	1.3 – 2	1.5	0.62	33.8	$33.0 \pm 1.0\%$	$32.8 \pm 1.0\%$	$15.4 \pm 0.5\%$
GIS	2 – 4	2.5	0.41	27.5	$32.0 \pm 1.0\%$	$31.7 \pm 1.0\%$	$15.4 \pm 0.5\%$
GIS	4 – 10	5	0.14	16.2	$29.7 \pm 0.9\%$	$29.0 \pm 0.9\%$	$16.3 \pm 0.6\%$
<i>RXTE</i>	2 – 4	3.3	0.78	14.0	$34.6 \pm 1.6\%$	$33.8 \pm 1.6\%$	$24.2 \pm 1.2\%$
<i>RXTE</i>	4 – 10	6	1.04	13.4	$33.5 \pm 1.6\%$	$32.6 \pm 1.6\%$	$23.9 \pm 1.2\%$

Table 3. Ton S180 Variability Parameters

Instrument	Energy Range (keV)	Band Center (keV)	Count Rate (c/s)	Signal to Noise	Total Variance	Fractional Variability	Point-to-Point Variability
<i>EUVE</i>	0.1 – 0.2	0.15	0.14	5.5	$28.3 \pm 1.7\%$	$17.8 \pm 2.7\%$	Undefined
<i>ASCA</i>	0.7 – 0.95	0.85	0.19	17.2	$20.3 \pm 1.1\%$	$19.4 \pm 1.1\%$	$7.2 \pm 0.6\%$
<i>ASCA</i>	0.95 – 1.3	1.1	0.37	21.5	$19.6 \pm 1.0\%$	$19.0 \pm 1.0\%$	$9.4 \pm 0.6\%$
<i>ASCA</i>	1.3 – 2	1.5	0.42	23.4	$17.8 \pm 0.9\%$	$17.2 \pm 1.0\%$	$9.6 \pm 0.6\%$
<i>ASCA</i>	2 – 4	2.5	0.25	18.0	$18.5 \pm 1.0\%$	$17.5 \pm 1.0\%$	$10.4 \pm 0.7\%$
<i>ASCA</i>	4 – 10	5	0.08	9.8	$19.4 \pm 1.0\%$	$16.2 \pm 1.2\%$	$9.3 \pm 1.1\%$
SIS	0.7 – 0.95	0.85	0.19	17.2	$20.3 \pm 1.1\%$	$19.4 \pm 1.1\%$	$7.2 \pm 0.6\%$
SIS	0.95 – 1.3	1.1	0.28	20.8	$18.6 \pm 1.0\%$	$17.9 \pm 1.0\%$	$8.5 \pm 0.6\%$
SIS	1.3 – 2	1.4	0.24	19.4	$18.3 \pm 1.0\%$	$17.5 \pm 1.0\%$	$9.8 \pm 0.7\%$
SIS	2 – 4	2.5	0.13	13.9	$19.1 \pm 1.0\%$	$17.5 \pm 1.1\%$	$10.9 \pm 0.8\%$
SIS	4 – 10	5	0.04	7.1	$21.2 \pm 1.1\%$	$15.5 \pm 1.5\%$	$8.6 \pm 1.7\%$
GIS	0.95 – 1.3	1.1	0.09	11.4	$24.7 \pm 1.3\%$	$22.9 \pm 1.4\%$	$11.6 \pm 1.0\%$
GIS	1.3 – 2	1.5	0.17	17.3	$17.9 \pm 0.9\%$	$16.8 \pm 1.0\%$	$9.4 \pm 0.7\%$
GIS	2 – 4	2.5	0.12	14.6	$18.7 \pm 1.0\%$	$17.3 \pm 1.1\%$	$9.3 \pm 0.8\%$
GIS	4 – 10	5	0.05	8.4	$20.0 \pm 1.1\%$	$15.8 \pm 1.3\%$	$9.1 \pm 1.3\%$
<i>RXTE</i>	2 – 4	3.3	0.11	6.1	$26.2 \pm 1.6\%$	$19.6 \pm 2.1\%$	$10.5 \pm 2.3\%$
<i>RXTE</i>	4 – 10	6	0.16	5.8	$28.9 \pm 1.7\%$	$22.1 \pm 2.2\%$	$12.8 \pm 2.3\%$

Table 4. Akn 564 Cross Correlation Results

Band 1 (keV)	Band 2 (keV)	DCF r_{max}	DCF τ (hr)	ICF r_{max}	ICF τ (hr)
0.85	1.1	0.97	0.0	0.97	0.0
0.85	1.5	0.94	0.0	0.94	0.0
0.85	2.5	0.91	0.0	0.92	0.0
0.85	5	0.85	0.0	0.85	0.0
1.1	1.5	0.99	0.0	0.99	0.0
1.1	2.5	0.97	0.0	0.97	0.0
1.1	5	0.91	0.0	0.91	0.0
1.5	2.5	0.99	0.0	0.99	0.0
1.5	5	0.94	0.0	0.94	0.0
2.5	5	0.97	0.0	0.97	0.0

Table 5. Ton S180 Cross Correlation Results

Band 1 (keV)	Band 2 (keV)	DCF r_{max}	DCF τ (hr)	ICF r_{max}	ICF τ (hr)
0.15	0.85	0.59	-1.6	0.63	0.0
0.15	1.1	0.54	0.0	0.61	+0.8
0.15	1.5	0.46	+1.6	0.54	+0.8
0.15	2.5	0.44	+1.6	0.49	+1.6
0.15	5	0.32	+4.8	0.35	+4.0
0.85	1.1	0.92	0.0	0.92	0.0
0.85	1.5	0.83	0.0	0.83	0.0
0.85	2.5	0.77	0.0	0.77	0.0
0.85	5	0.48	0.0	0.49	0.0
1.1	1.5	0.92	0.0	0.92	0.0
1.1	2.5	0.84	0.0	0.84	0.0
1.1	5	0.61	0.0	0.62	+0.8
1.5	2.5	0.90	0.0	0.90	0.0
1.5	5	0.72	0.0	0.72	0.0
2.5	5	0.72	0.0	0.73	+0.8

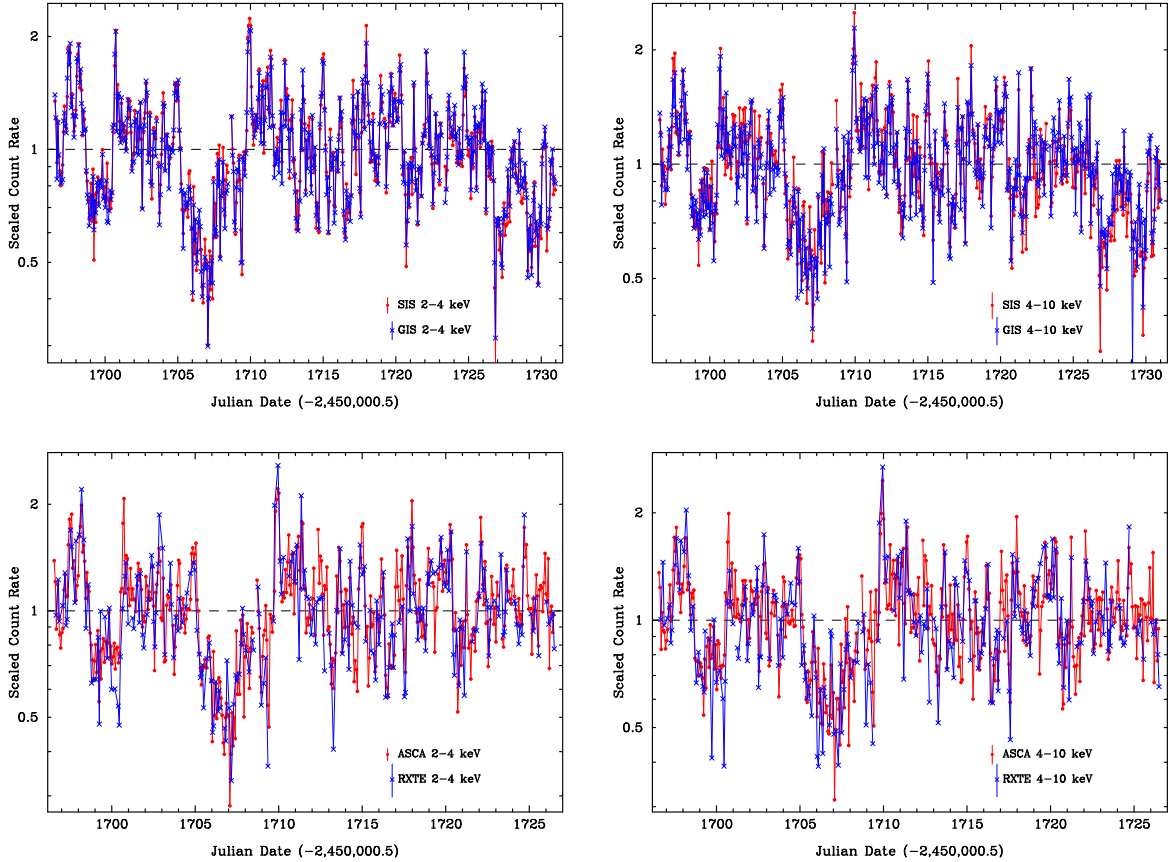


Fig. 1.— Light curve overplot diagrams for Akn 564. All data were scaled by dividing by the mean of that light curve to eliminate the effects of differing instrumental sensitivities. In the upper left, the 2-4 keV *ASCA* SIS (red, circles) and GIS (blue, triangles) light curves are shown, in the upper right, the 4-10 keV SIS and GIS light curves, in the lower left, the 2-4 keV summed *ASCA* (red, circles) and *RXTE* (blue, triangles) light curves, and in the lower right, the 4-10 keV summed *ASCA* and *RXTE* light curves. Note the good agreement between the *ASCA* SIS and GIS data (also seen in lower energy bands), while the *RXTE* data does not agree as well.

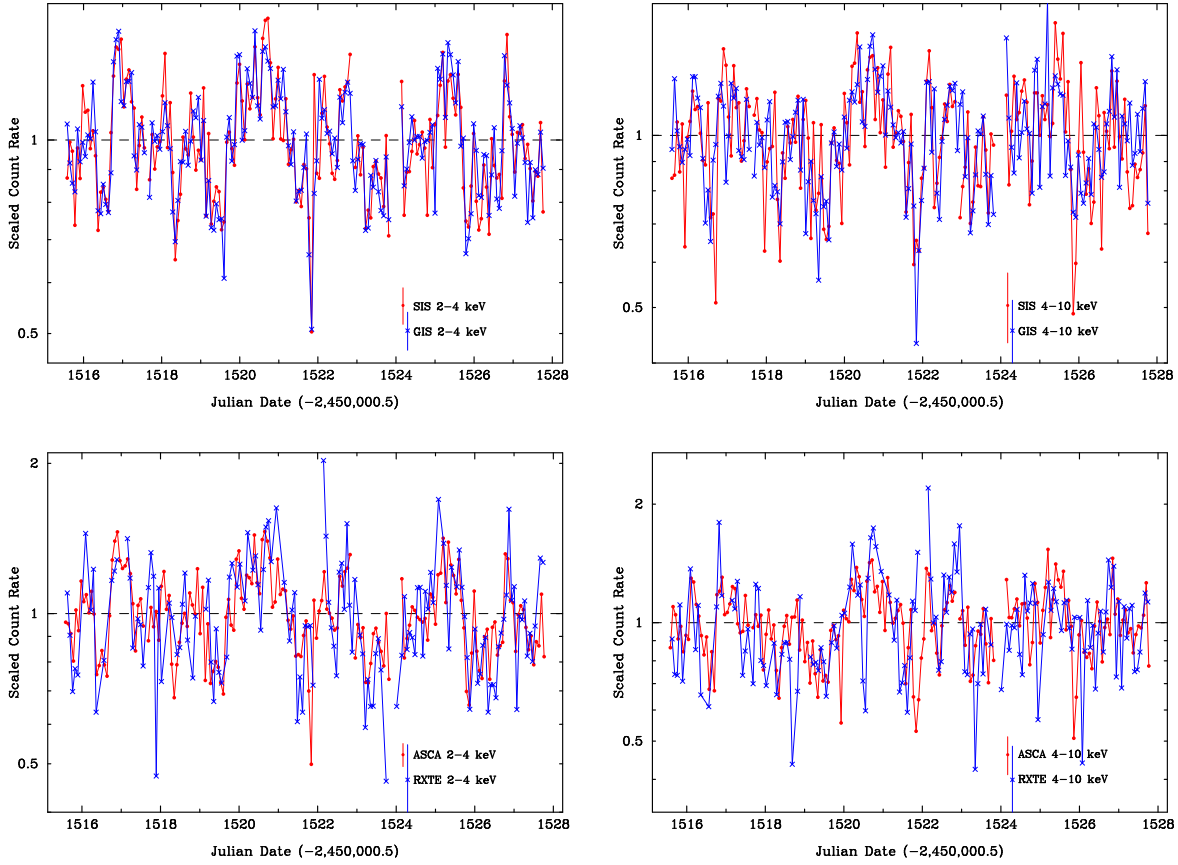


Fig. 1.— Same as Figure 1a, but for Ton S180. Note the good agreement between the *ASCA* SIS and GIS data, but relatively poor agreement between the *RXTE* and *ASCA* quasi-simultaneous data.

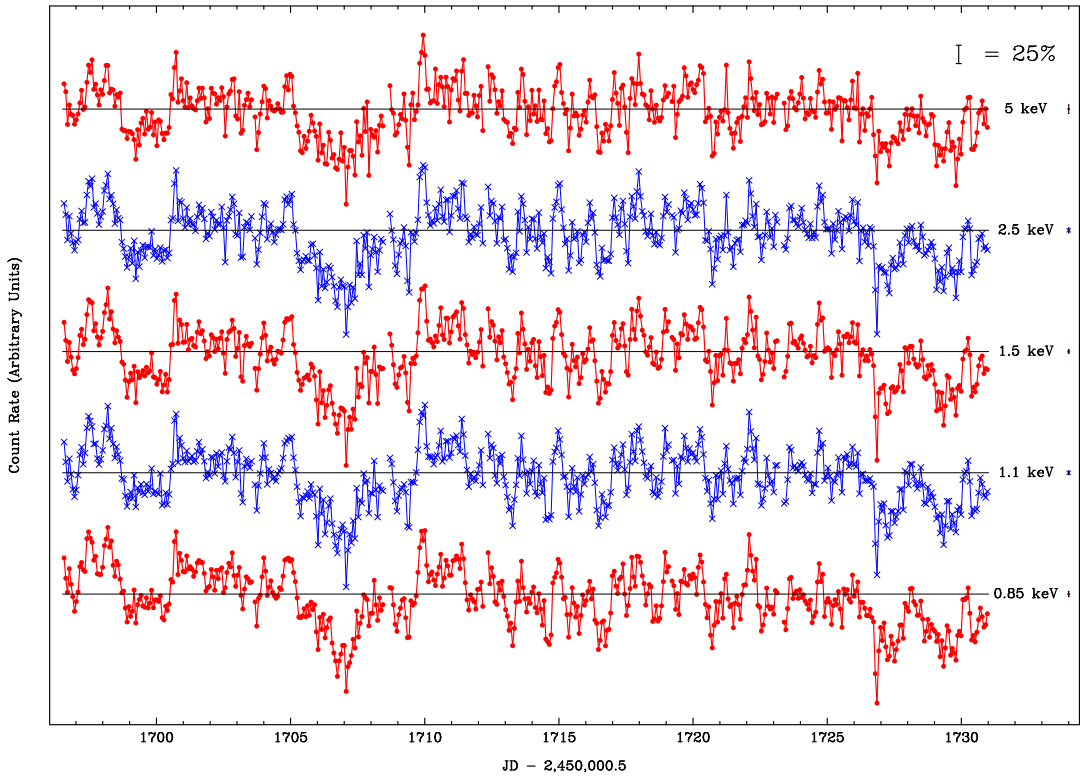


Fig. 2.— Light curves for Akn 564, covering from top to bottom, 5 keV, 2.5 keV, 1.5 keV, 1.1 keV and 0.85 keV. As the data are presented in logarithmic units, with an arbitrary offset between bands, a 25% change is shown in the upper right. Error bars are not shown because the figure would become too crowded, so typical 1σ errors are shown on the right. Lines connect the points only for adjacent orbits, so a broken line indicates that an orbit was missing.

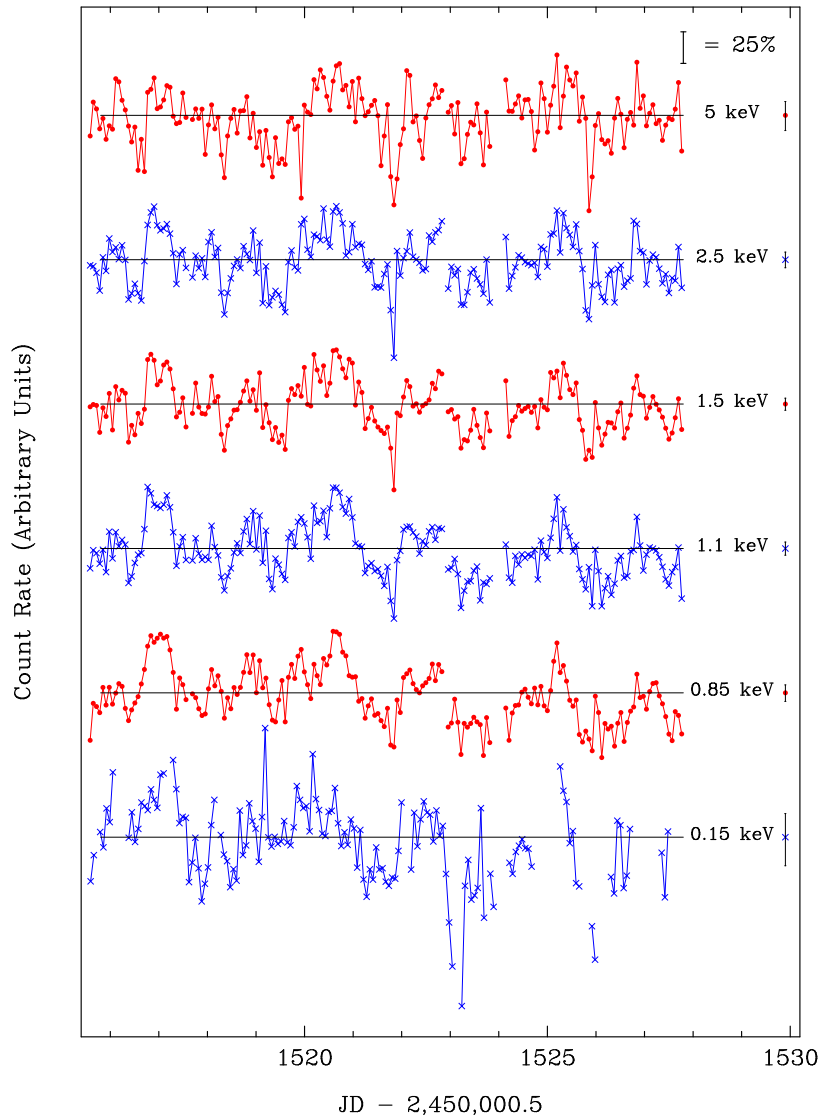


Fig. 2.— Same as Figure 2a, but for Ton S180. The bottom light curve is for *EUVE* 0.15 keV.

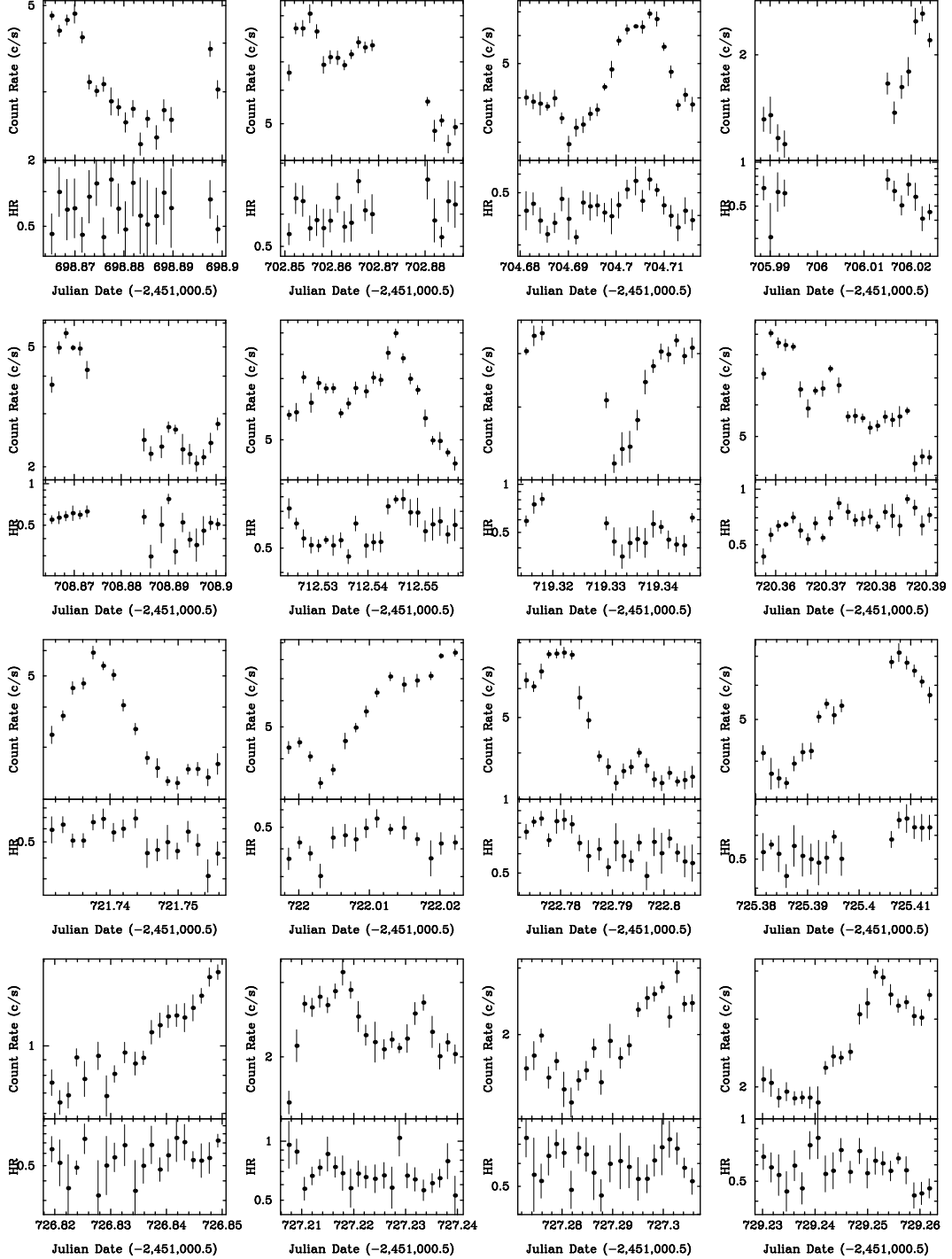


Fig. 3.— Single orbit light curves for Akn 564. The total 0.7–10 keV count rate is shown on the top and the 2–10 keV/0.7–1.3 keV hardness ratio on the bottom. The 16 orbits in which a factor of ≥ 2 flux variation are plotted. The plots are ordered by time.

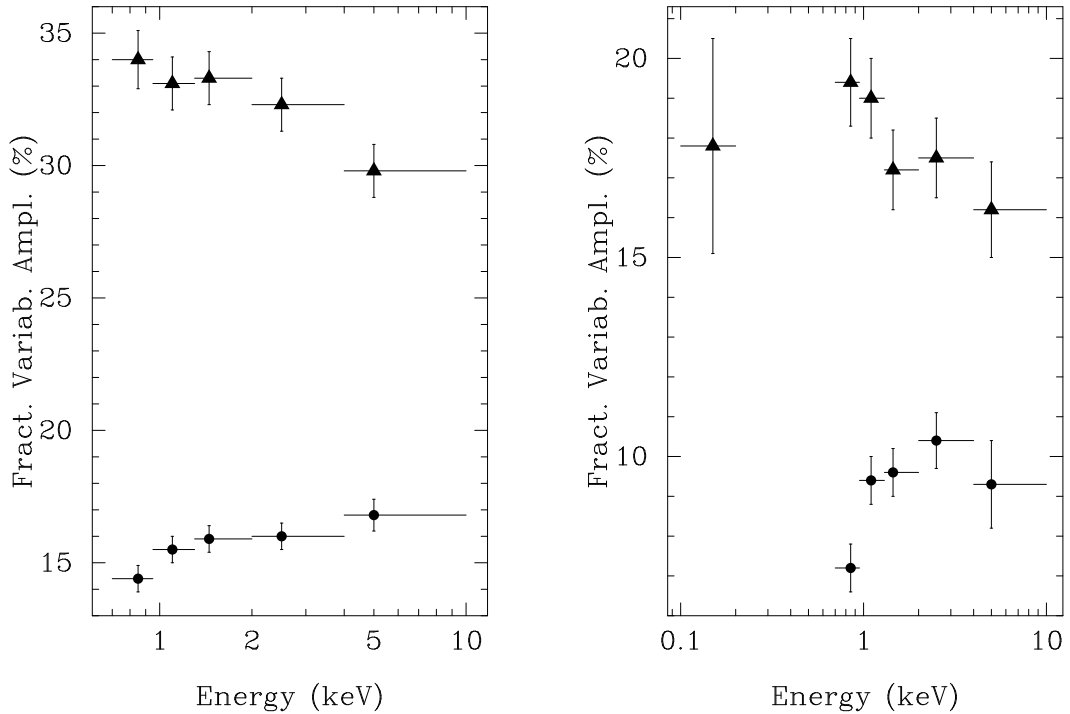


Fig. 4.— Fractional variability (F_{var}) and orbit-to-orbit variability amplitudes (F_{pp}) in different energy bands for Akn 564 (left) and Ton S180 (right). The filled triangles refer to F_{var} , the fractional variability amplitude, corrected for the effect of measurement noise, and the filled circles refer to F_{pp} , the point-to-point variability amplitude, also corrected for noise. The error bars are derived as in the Appendix. For the *EUVE* observations of Ton S180, F_{pp} is undefined (that is, the measured variance is marginally smaller than that expected from measurement noise alone), so no point is plotted.

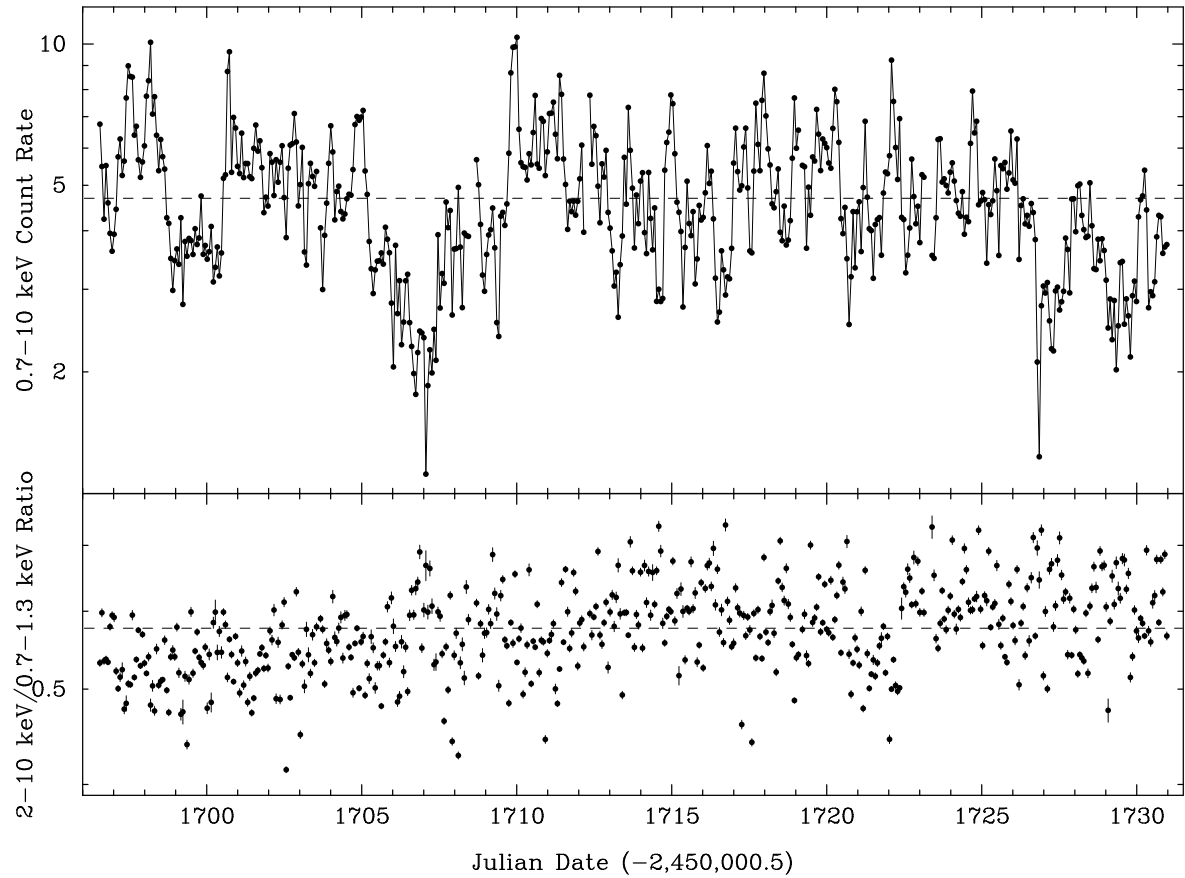


Fig. 5.— Orbitally-binned flux and hardness ratio light curves for Akn 564. The top panels show the 0.7–10 keV light curve while the bottom panels show the 0.7–1.3 keV/2–10 keV hardness ratio. The error bars are not shown on the fluxes; they are about the size of or a bit bigger than the plotting symbols (typically ~ 0.08 ct/sec).

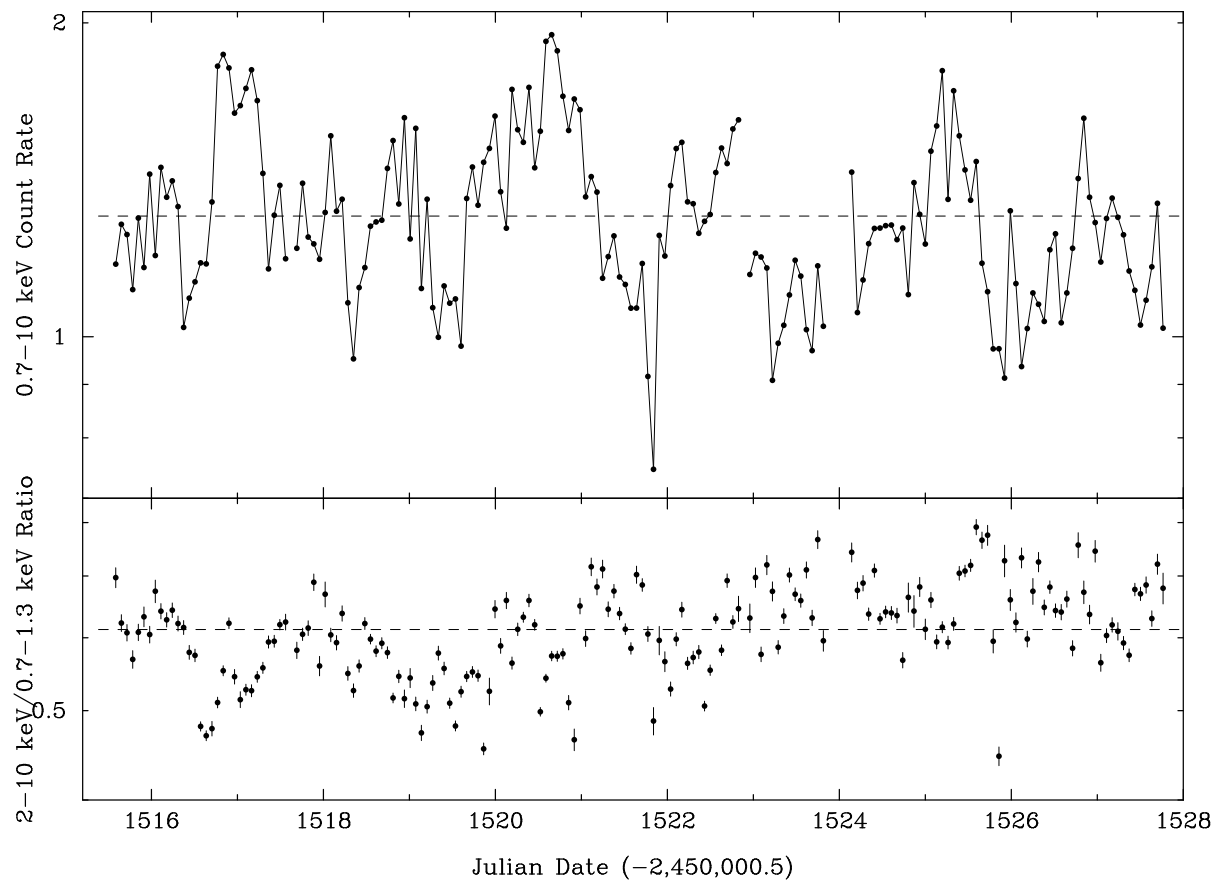


Fig. 5.— Same as Figure 5a, but for Ton S180. The error bars on the count rates are typically ~ 0.03 ct/sec.

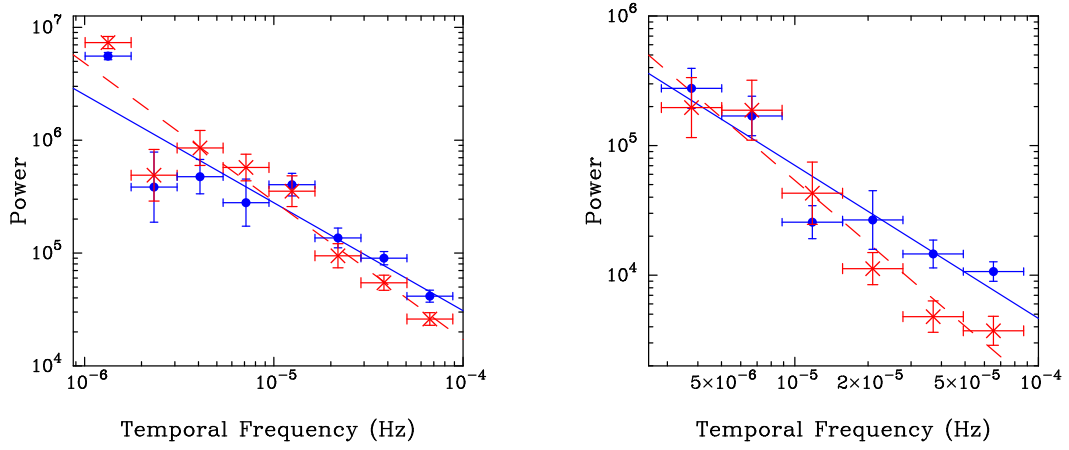


Fig. 6.— PDS for Akn 564 (left) and Ton S180 (right). The 0.85 keV data are denoted in red by \times s and a dashed-line power-law fit, while the 5 keV data are denoted in blue by circles and a solid-line power-law fit.

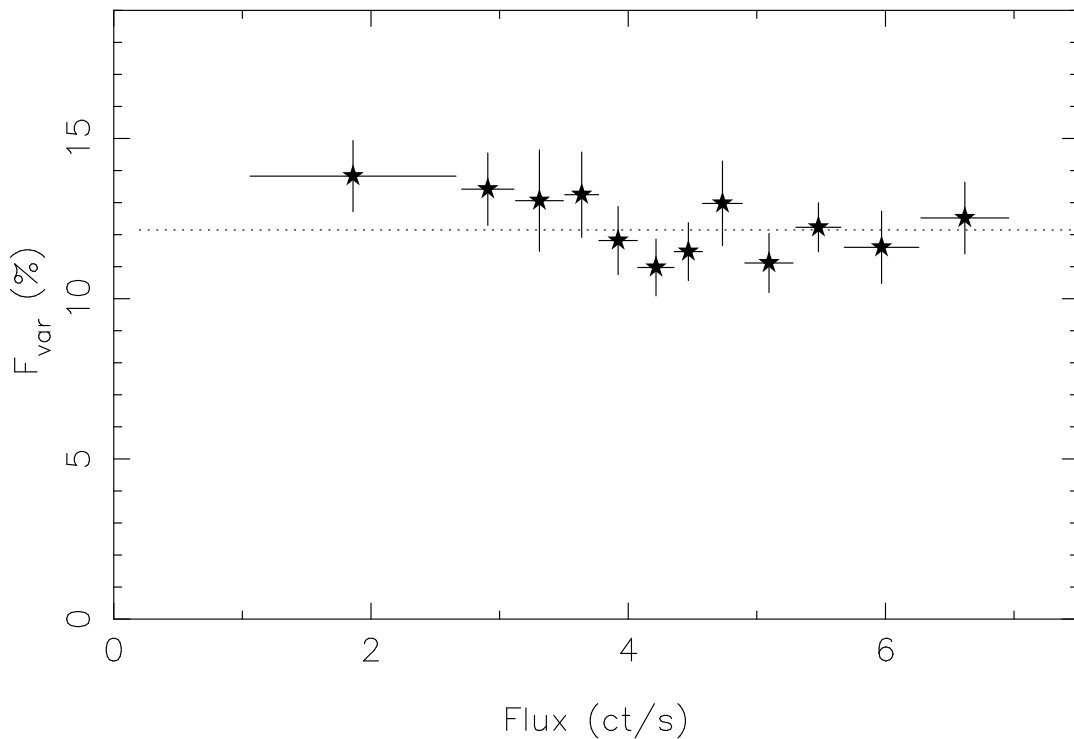


Fig. 7.— Fractional variability amplitude binned as a function of mean count rate for the 256 Akn 564 orbits with more than 32 min of data. As discussed in the text, the data were binned by flux such that each bin has at least 20 orbital points.

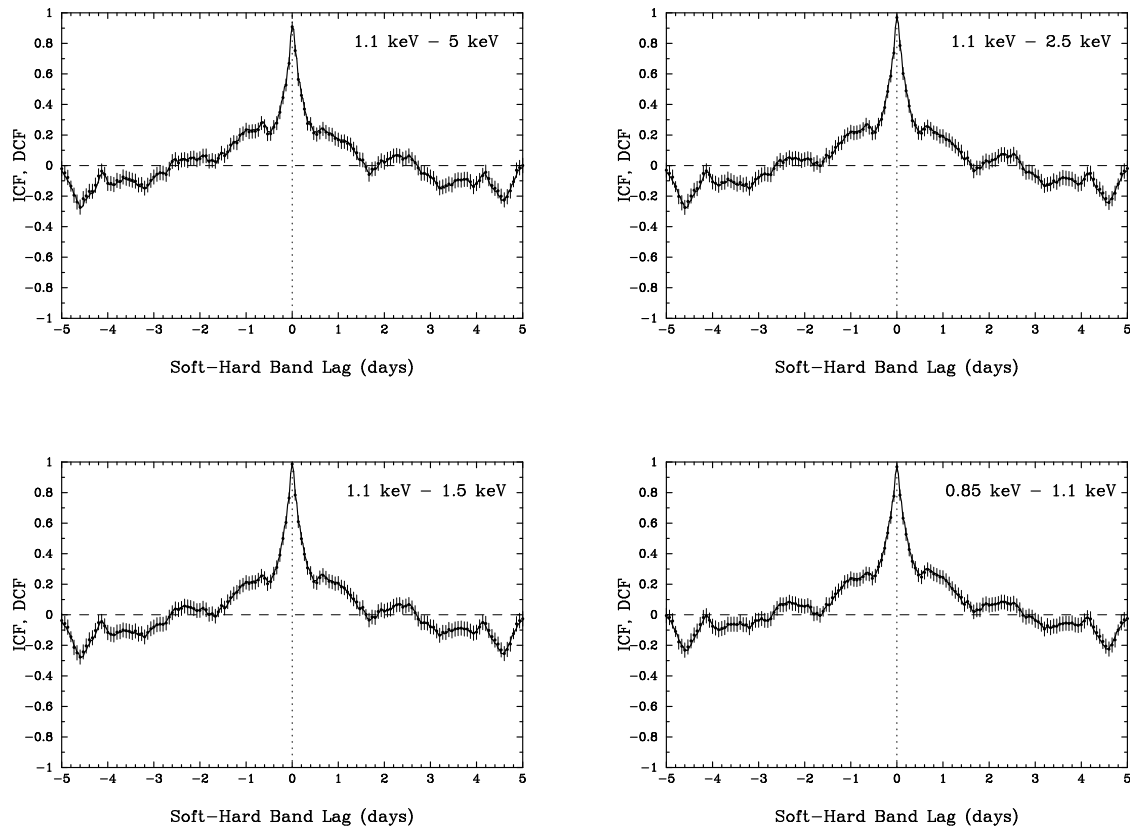


Fig. 8.— Cross-correlation functions for Akn 564. The solid line refers to the ICF, while the circles with error bars are DCF. All are referenced to 1.0 keV, in the sense that a positive peak would mean that the softer band leads the harder. The top panel is the CCF with 5 keV, next with 2.5 keV, next with 1.5 keV, and at the bottom, with 0.7 keV.

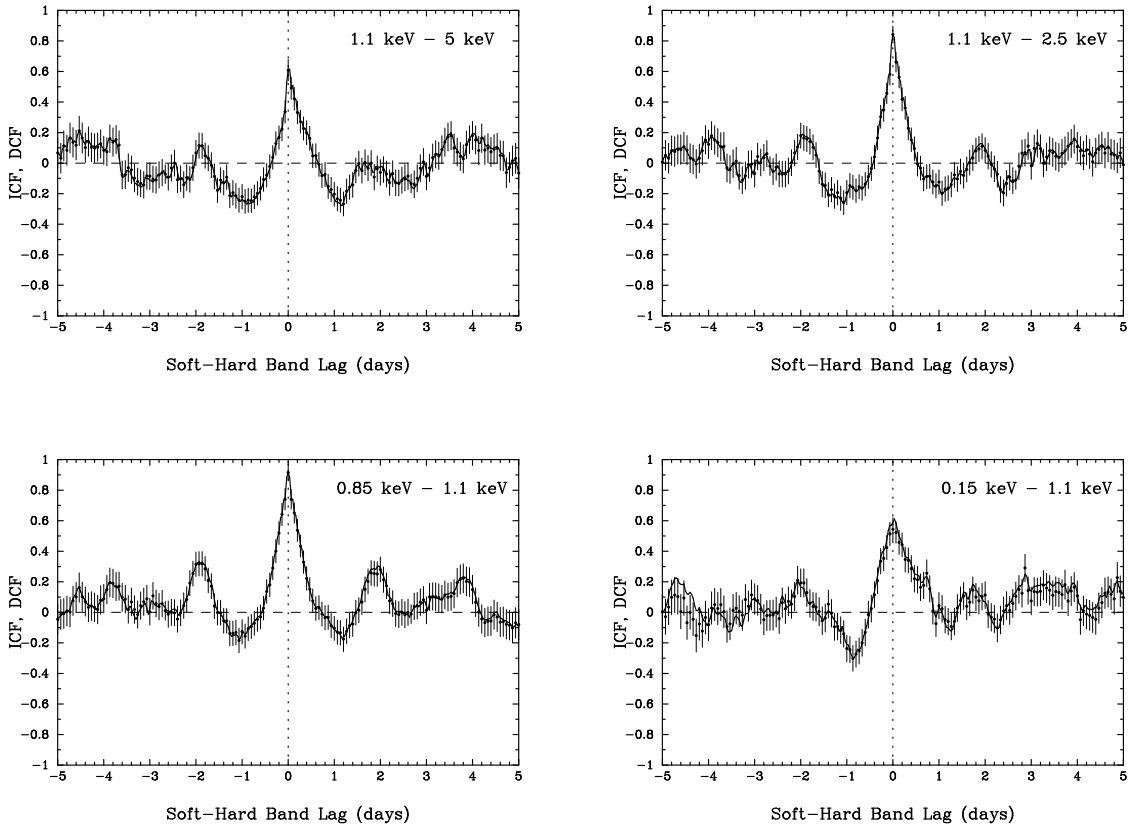


Fig. 8.— Same as Figure 8a, except for Ton S180, and that the *ASCA* 1.0 keV and *EUVE* 0.15 keV band CCF is shown instead of the *ASCA* 0.85 keV–1.5 keV CCF.